Journal of Materials Chemistry A

ROYAL SOCIETY OF CHEMISTRY

REVIEW

View Article Online
View Journal | View Issue

Cite this: J. Mater. Chem. A, 2023, 11, 4836

CZTSSe solar cells: insights into interface engineering

Yimeng Li,[ab] Hao Wei,[ab] Changcheng Cui,[a] Xiao Wang,[ac] Zhipeng Shao, *[ac] Shuping Pang *[ac] and Guanglei Cui *[ac]

Received 8th December 2022
Accepted 31st January 2023

DOI: 10.1039/d2ta09561k

rsc.li/materials-a

$Cu_2ZnSn(S,Se)_4$ (CZTSSe) photovoltaic (PV) technology has attracted much attention due to its cost efficiency, non-toxic nature, and use of earth-abundant elements. However, the current world record power conversion efficiency (PCE) of CZTSSe solar cells is 13.0%, lagging far behind the 23.4% of its predecessor $Cu(In,Ga)Se_2$ (CIGS). The open-circuit voltage (V_{OC}) deficit is always the key factor for the unsatisfactory efficiency of CZTSSe solar cells and is mainly related to the mismatch of the energy-band structure and deep-level defects at the interfaces. In this review, the current problems at the interfaces are discussed and recent works on interface engineering are summarized. Finally, we present our views on the challenges and prospects in this field.

1. Introduction

From the global market perspective, crystalline silicon solar cells will remain the mainstream photovoltaic market in the short term. Still, the transition toward thin-film solar cells and other new types of solar cells with low cost and environment friendliness has become an inevitable trend.[1–5] Compared with crystal silicon solar cells, thin-film solar cells have greater scope for cost reduction and can be embedded in building-attached photovoltaic (BAPV) and building-integrated photovoltaic (BIPV) applications.[6–8] Chalcogenide CdTe and CIGS solar cells have demonstrated efficiencies of over 20% and long-term stability and have been commercially available for decades.[9,10] From a sustainability perspective, CdTe and CIGS solar cells can hardly dominate the PV market, mainly due to the scarcity of Te, In, and Ga.[11–14] High abundance, low-priced, and eco-friendly semiconductors are thus needed for high-performance thin-film solar cells.[15–17] By replacing In and Ga with inexpensive, abundant, and non-toxic Zn and Sn, CZTSSe solar cells are currently considered one of the best choices.[18–20]

CZTSSe films have advantages in the following aspects:[21–25] element abundant reserves, low price, and environmental friendliness, which give the future commercialized CZTSSe solar cells a significant advantage in manufacturing costs and sustainable development potential.[5,26] Furthermore, CZTSSe is a stable direct bandgap p-type semiconductor material with a bandgap that varies in the range of 1.0 to 1.5 eV depending on the S/Se ratio, which matches the standard solar spectrum very well.[15,27] In addition, CZTSSe has an absorption coefficient of up to the order of 10^4 cm^{-1}, while only 1–2 microns are needed for full light absorption.[27,28] The excellent photovoltaic property of CZTSSe allows it produce high-efficiency multi-junction thin-film solar cells combined with GaAs or perovskite solar cells.[27,29,30]

However, the current record efficiency of CZTSSe solar cells is 13.0% (V_{OC} = 529.4 mV, short-circuit current density (J_{SC}) = 33.6 mA cm^{-2}, fill factor (FF) = 72.9%), which is far from the 23.4% of the high-performance CIGS solar cells (V_{OC} = 734.0 mV, J_{SC} = 39.6 mA cm^{-2}, FF = 80.4%). The V_{OC}, J_{SC}, and FF of the best-performing CZTSSe solar cell are only 59.7%, 80.2%, and 81.9% of the theoretical values, which are much lower than the corresponding values for CIGS.[27,31,32] The difference between CZTSSe and CIGS comes mainly from the V_{OC} deficit caused by the severe charge recombination in CZTSSe devices.[33–36] As a five-membered material, CZTSSe has more self-interstitial vacancies and defect clusters than binary and ternary semiconductor materials. Due to the similar chemical properties of Cu (1.32 Å) and Zn (1.22 Å) and their similar ionic radii, the absorbing materials are prone to defects with a low formation energy. Calculations based on density functional theory (DFT) showed the presence of vacancies in the material: V_{Zn}, V_{Cu}, V_{Sn}, antisite defects: Cu_{Sn}, Cu_{Zn}, Sn_{Zn}, defect clusters: V_{Cu} + Zn_{Cu}, V_{Zn} + Sn_{Zn}, Zn_{Sn} + $2Zn_{Cu}$, *etc.* The simulations showed that V_{Cu} and Cu_{Zn} defects have a small formation energy, which is the underlying reason for the more significant concentration of Cu_{Zn} defects in the p-type CZTSSe semiconductor.[37,38] Deep energy level defect states in the bulk phase lead to severe band tail states in the material, which act as recombination centers, leading to non-radiative recombination that reduces the solar cell carrier lifetime. Compared to CIGS solar cells, CZTSSe solar

[a]Qingdao Industrial Energy Storage Research Institute, Qingdao Institute of Bioenergy and Bioprocess Technology, Chinese Academy of Sciences, 266101 Qingdao, P. R. China. E-mail: shaozp@qibebt.ac.cn; pangsp@qibebt.ac.cn; cuigl@qibebt.ac.cn

[b]Center of Materials Science and Optoelectronics Engineering, University of Chinese Academy of Sciences, 100049 Beijing, P. R. China

[c]Shandong Energy Institute, 266101 Qingdao, P. R. China

cells have poor carrier-transport capabilities due to interfacial recombination.[39] It was also found that the individual interface recombination in CZTSSe solar cells is influenced by several factors, such as energy level matching, interface defects, and the carrier concentration of the absorber layer and other contact materials.[33,39,40] In conventional CZTSSe solar cells, there are two dominant interfaces from the front electrode to the Mo back electrode: (1) the CZTSSe/CdS interface, known as the front interface and (2) the Mo/CZTSSe interface, known as the back interface.[33] The interface determines the carrier separation, collection, and recombination. Interface engineering is an effective way of suppressing interfacial recombination and improving the V_{OC}. It is essential to assess the relevant properties of the interface, the mechanisms of recombination at different interfaces, and the collection of charge carriers at the interface.[6,11,23,33,41]

This review provides insights into interface engineering and the strategies employed at the interfaces, divided into three sections. The first section mainly presents the problems and solutions at the back interface, and this section contains two branches: the blocking layer and the sacrificial layer. In the second section, the problems at the front interface and the efforts made on these problems are described and analyzed in detail. This section includes the following points: the passivation layers, alternative buffer layers, and heterojunction annealing. Finally, we present our views on the challenges and prospects in this field and discuss proposals for further improvements in interface engineering for CZTSSe solar cells.

2. Interface engineering

2.1 Back interface

2.1.1 Recent problems at the back interface. The Mo back-contact is the most widely used as the back electrode of CIGS solar cells, but it is still a big challenge in CZTSSe solar cells.[42,43] There are three main problems at the back interface: the formation of the interfacial layer $MoS(e)_2$, secondary phases, and pinholes.[44–47] The formation of the $MoS(e)_2$ process and the equilibrium S(e) vapor pressure *versus* the annealing temperature for the reactions are shown in Fig. 1a and b. Fig. 1a shows that the formation of the interfacial $MoSe_2$ layer is mainly limited by the diffusion of Se vapor through the absorber layer, which is the rate-determining step in the formation of the $MoSe_2$ layer. The thickness of the $MoSe_2$ layer increases with increasing the selenization temperature and time, demonstrating the time and temperature dependence of the $MoSe_2$ layer thickness.[48] Fig. 1b shows the secondary phase-evolution pathways revealed by thermodynamic studies during sulfurization and selenization. During sulfurization, the equilibrium vapor pressure of S on SnS and Cu_2S is much higher than that of ZnS, suggesting that the sulfurization of monolithic Zn is easier than that of Sn and Cu. However, in the case of the selenization process, even if the selenization curve of elemental Zn is at the lower pressure point, the replacement of the S atom by Se atom in ZnS seems to be difficult at the high-pressure point.[49] The pinholes at the back interface of the CZTSSe solar cell are shown in Fig. 1c.[50]

Detailed thermodynamic investigations were reported by Scragg *et al.*,[51] who indicated that the Mo/CZTSSe interface exhibits lower chemical stability than Mo/CIGS. The net free energy change (ΔG) associated with the absorber layer measured at 550 °C showed that ΔG is positive for CIGS while negative for CZTS and CZTSe at -150 kJ mol^{-1} and -100 kJ mol^{-1}, respectively, indicating the instability nature of CZTSSe during the thermal annealing. The following side reactions occur at the back interface during the selenization process.

$$2Cu_2ZnSnS(e)_4 + Mo \rightarrow 2Cu_2S(e) + 2ZnS(e) + 2SnS(e) + MoS(e)_2$$

$$Se_{(g)} + Mo \rightarrow MoS(e)_2$$

The side reactions form the secondary phases and bring in defects at the CZTSSe/Mo interface. While every coin has two sides. A thinner $MoSe_2$ interfacial layer not only facilitates the formation of ohmic contacts at the back interface but also allows for increased adhesion between Mo and CZTSSe layers.[23,52] Cozza *et al.*[53] demonstrated through theoretical simulations and experimental results that an appropriately thick $MoSe_2$ interfacial layer is a prerequisite for the preparation of highly efficient devices. However, as mentioned above, due to the back interface instability during selenization and excessive amounts of selenium, excessively thick $MoSe_2$ interfacial layers are often generated, which can be hundreds or thousands of nanometers thick, resulting in increased series resistance (R_S) and reduced FF values of the cells.[54] The thick $MoSe_2$ layer can also act as a carrier scattering center, exacerbating back-interface recombination,[55] even when the absorber layer has excellent crystalline quality.[56–58]

The side reactions also lead to pinholes.[44,59] The continuous removal of gaseous byproducts [SnS(e) and ZnS(e)] from the annealed environment during sulfurization or selenization creates pinholes at the interface.[34,51] Similarly, pinholes are also formed due to the Kirkendall effect between elemental copper and its sulfide or selenide derivatives [*i.e.*, CuS(e)] during the high-temperature thermal annealing process.[23] The Cu element exhibits a higher diffusivity than S, thus forming pinholes, and these pinholes can rupture again *en masse* to form larger pinholes at the Mo/absorber interface.[18]

Optimizing the properties of the back interface is critical to improving the device performance. Researchers have introduced numerous interfacial layer materials at the back interface, and the current state of research in this area is shown in Table 1. Here we classified the interfacial layers into two categories depending on their properties: the blocking layer, where the interfacial layer material does not participate in the reaction in the selenization process;[42,44,58,60–66] and the sacrificial layer, which is introduced to take part in the reaction during selenization.[43,46]

So far, there is currently no universal back-interface engineering solution to significantly improve the efficiency of CZTSSe solar cells. Further refining of the experimental design and exploring a more suitable back-interface interlayer to

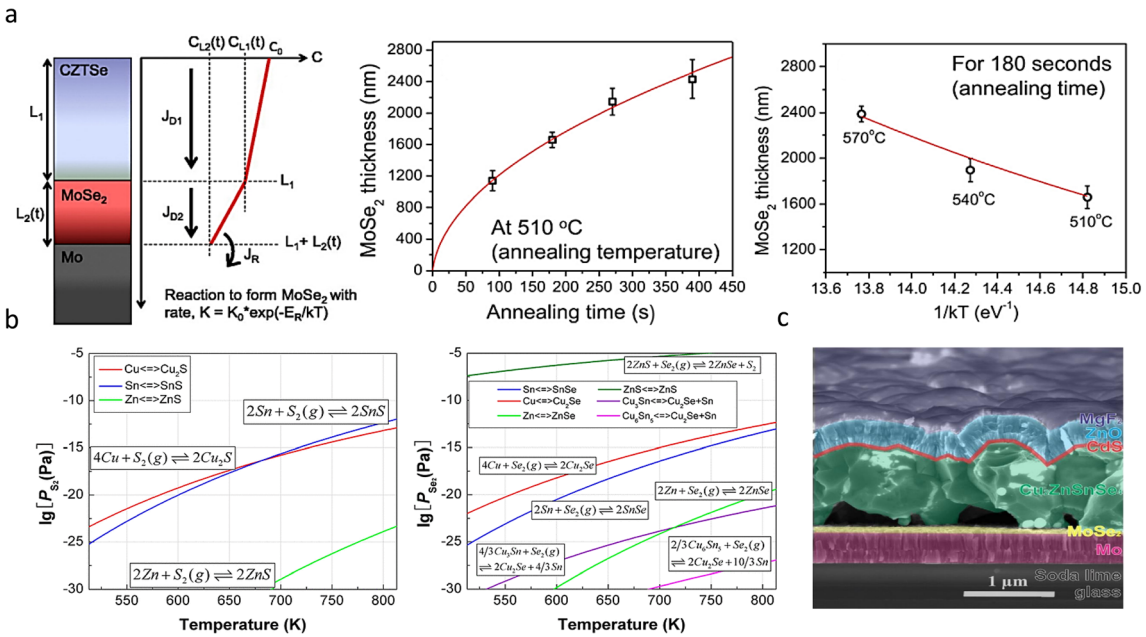

Fig. 1 (a) Schematic diagram of Se diffusion through CZTSSe/$MoSe_2$/Mo during high-temperature annealing.[48] Reproduced with permission from ref. 48. (b) Equilibrium S vapor pressure *vs.* sulfurization temperature for the reactions and equilibrium Se vapor pressure *vs.* selenization temperature for the reactions.[49] Reproduced with permission from ref. 49. (c) Pinholes at the back interface of the CZTSSe solar cell.[50] Reproduced with permission from ref. 50.

optimize CZTSSe thin-film solar cells are thus needed in the following research.

2.1.2 Blocking layer. The blocking layers are mostly thin films that are stabilized in a high-temperature selenium atmosphere, such as MoO_3,[69,72–74] Al_2O_3,[47,67,75,76] TiN,[44,61,68] and Si_xN_y.[60] The blocking layers block the diffusion of Se to the back-contact during the selenization process, thus avoiding the Se/Mo reaction and reducing the back-interface secondary phases and pinholes. A suitable thickness of the blocking layer is needed for effective hole tunneling.

Al_2O_3 is a shining star among the many blocking layers due to its unique advantage. Liu *et al.* reported that by introducing an Al_2O_3 interlayer between Mo and CZTS, the interfacial reaction between CZTS and Mo is suppressed at the early stage of sulfuration, and that pinholes and phase segregation in the back-contact region can be well eliminated. The addition of the Al_2O_3 blocking layer increases the conversion efficiency of the ultrathin CZTS solar cell from 7.34% to 8.56%. Also, this back-interface contact was proved to be effective and reproducible in normal-thickness CZTS devices.[67] The chemically inert

Table 1 Representative work of the back-interface engineering of CZTSSe

Categories	Absorber	Intermediate layer	V_{OC} (mV)	J_{SC} (mA cm^{-2})	FF (%)	PCE (%)	References
Blocking layer	CZTS	Al_2O_3	657	19.8	65.9	8.6	67
		w. o. Al_2O_3	632	19.0	61.1	7.3	
	CZTSe	MoO_2	393	32.6	63.6	8.2	68
		w. o. MoO_2	385	31.8	59.6	7.3	
	CZTSSe	MoO_3	465	37.9	64.0	11.3	69
		w. o. MoO_3	399	—	—	8.4	
	CZTS	AZO	681	19.5	63.4	8.4	58
		w. o. AZO	665	18.8	57.1	7.1	
	CZTSSe	C	514	38.2	68.8	13.5	63
	CZTSe	TiN	385	42.6	54.2	8.9	70
		w. o. TiN	264	25.4	44.0	3.0	
Sacrificial layer	CZTSSe	VSe	332	28.7	46.2	4.4	71
		w. o. VSe	389	28.4	55.6	6.2	
	CZTS	Na_2S	337	12.7	53.6	2.3	43
		w. o. Na_2S	330	10.4	34.5	1.1	
	CZTSSe	GeO_2	547	70.0	34.3	13.1	46
		w. o. GeO_2	496	68.0	33.6	11.3	

conductor titanium nitride (TiN) effectively passivates the Mo/CZTS interface and can block the interfacial reaction between Mo and S in the annealing atmosphere, whereas Na transport from the substrate is unaffected, as shown in Fig. 2a. Unfortunately, the TiN/CZTS contacts generate a relatively high series resistance.[44] Therefore, further research is needed to develop blocking layers with better properties. Recently, many researchers have concluded that MoO_3 is an ideal blocking layer for the Mo/CZTSSe interface.[69,72–74] Currently, the main methods for introducing MoO_3 interfacial layers are: (i) high-temperature annealing, (ii) magnetron sputtering, (iii) thermal evaporation, and (iv) spin coating. In 2019, Yu *et al.* found that the multilayer crystalline behavior of CZTSSe was induced by the formation of a secondary phase at the back interface, which was a chemical reaction between Mo and CZTSSe. An *in situ*-grown MoO_3 isolation layer was successfully introduced to block the reactions. They further found that, in addition to MoO_3, other materials such as SiO_2, TiN, and $MoSe_2$, were also effective in eliminating multilayer crystallization, as shown in Fig. 2b.[69] The insertion of a p-type contact MoO_3 with a high work function between the CZTSSe and Mo electrodes not only blocked the occurrence of back-interface side reactions but also enabled the formation of an interfacial field, which accelerated carrier separation, as shown in Fig. 2c.[74] Recently, Sun *et al.* used the porous MoO_3 array structure as a post-interface contact and elaborated on the effect of the MoO_3 microstructure on CZTSSe photovoltaic devices. This interpenetrating structure of the porous array not only helped to create a favorable interfacial field for effective carrier separation but also increased the interfacial contact area to extend the light propagation path through porous scattering and accelerated the aggregation of holes along the hole walls toward the Mo electrode, as shown in Fig. 2c.[74]

An emerging blocking layer has recently received much attention. The *in situ* interface layer is mainly the C-rich layer that remains from the selenization process.[63–65] Mercaptoethanolic acid (TGA)-amino aqueous solutions are susceptible to a CZTSSe grain phase bias growth behavior during selenization driven by the presence of a conductive carbon framework layer and the thermodynamic properties of the non-homogeneous thin-film system. A C-rich layer can play an essential role in improving the electrical contact between CZTSSe and Mo, allowing the formation of an ohmic contact at the absorption layer/Mo interface, thus enhancing the PCE of CZTSSe solar cells.

In 2021, an aqueous solution of ammonium thioacetate (ATGL) was reported by D. Hauschild *et al.*, and they obtained a 'buried' back-contact interface by cleavage in a liquid nitrogen environment.[64] This work presented a detailed picture of the chemical structure of this carbon-rich layer at the back-contact, which consisted of carbon (74 ± 7%), selenium (19 ± 4%), and sulfur (7 ± 3%). The selenium in this layer was in the form of elemental inclusions. The sulfur content of this carbon-rich layer was twice as high as that of the absorber. Detailed analysis of the chemical environment indicated that residues of the aqueous ATGL solution were the source of sulfur in this carbon-rich layer. In addition, S–Mo bonds were found beneath the carbon-rich layer at the back-contact of Mo; the specific data are shown in Fig. 3a. In the same year, the existence of a conductive carbon framework layer was explained more clearly by Xu *et al.*,

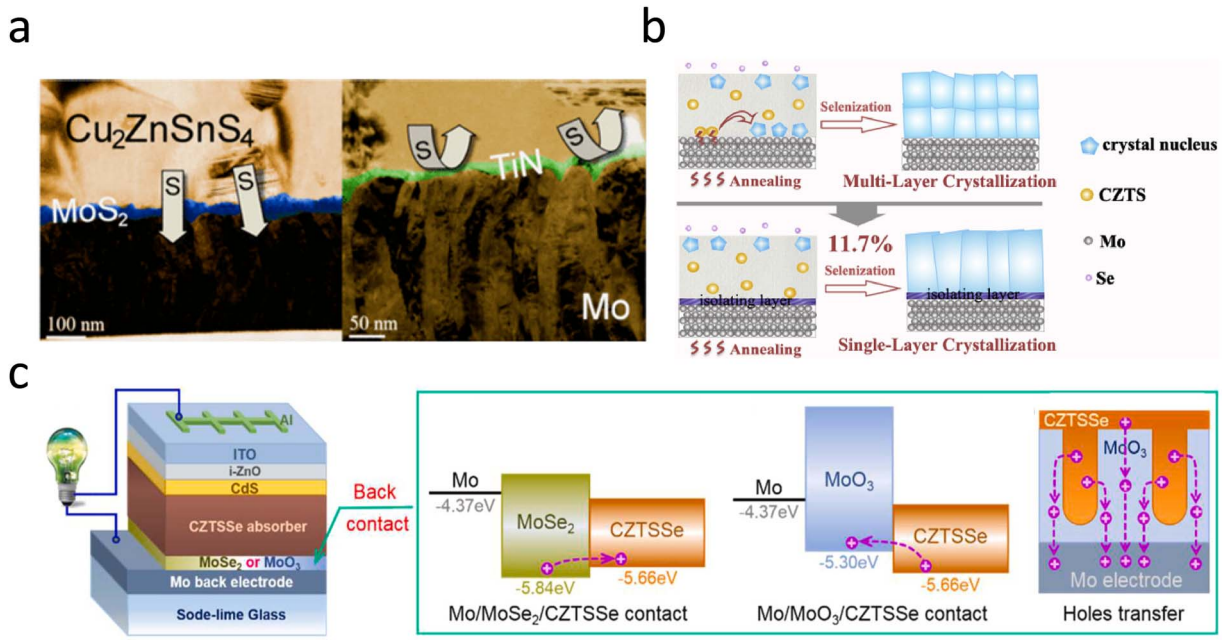

Fig. 2 (a) Schematic diagram of TiN action in the high-temperature annealing process.[44] Reproduced with permission from ref. 44. (b) Diagram of grain growth without and with MoO_3 blocking layer.[69] Reproduced with permission from ref. 69. (c) The structure diagram of the CZTSSe solar cell, the band diagram of Mo/$MoSe_2$/CZTSSe and Mo/MoO_3/CZTSSe, and the boundary face transfer diagram of interpenetrating MoO_3/CZTSSe arrays.[74] Reproduced with permission from ref. 74.

and schematic diagrams of the TGA-ammonia method and the energy-band structure of the cell are shown in Fig. 3b.[63] The interconnected mesoscopic carbon framework was mainly formed by large metal–organic clusters induced by the Sn-TGA coordination structure. The Sn had a six-coordinated design, and the deprotonated TGA had a double-coordinated end group.[77–79] The carbon layers could buffer the elemental composition fluctuations of the top CZTSSe grains by accommodating residual metallic elements or secondary phases on the one hand and facilitated the charge transport of the cell by improving the mechanical and electrical contact between the CZTSSe and Mo electrodes on the other.

2.1.3 Sacrificial layer. The sacrificial layer (such as Ag,[80,81] Na_2S,[43] GeO_2 (ref. 46)) undergoes a chemical reaction during the selenization process, and the sacrificial layer material decomposes and diffuses into the absorber layer or the back interface. By reducing the secondary phases and pinholes at the back interface, the material performance of the absorber layer can be improved.

In earlier studies, researchers found that sodium–calcium glass as a base material for CZTSSe solar cells could significantly improve the performance.[82–84] This was mainly due to the diffusion of Na into the absorber layer during high-temperature selenization to passivate the defects and enhance the absorber layer's crystal quality.[85,86] Since then, sodium doping has been of interest to researchers.[87–90] In 2018, Gu *et al.* found that the insertion of a Na_2S self-consuming layer could effectively stabilize the CZTS/Mo interface. A schematic diagram of the CZTS solar cells is shown in Fig. 4a. This eliminates the side reaction between CZTS and Mo, thereby improving the crystallinity of the CZTS absorbing layer, enhancing carrier transport at the CZTS/Mo interface, and reducing the series resistance.[43] In addition, the self-consumption property of the Na_2S sacrificial layer also averts the holes-transport barrier. Recently, Wang *et al.* developed a convenient and effective method to simultaneously design CZTSSe absorbers with back interfaces and bulk defects by introducing a GeO_2 layer on a Mo substrate, as shown in Fig. 4b.[46] Based on the optimum GeO_2 concentration, the CZTSSe device achieved a PCE of up to 13.14% with a V_{OC} of 547 mV. Further studies have shown that when selenization occurs, bidirectional diffusion co-occurs in the upward CZTSSe absorber layer and downward in the $MoSe_2$ layer. A portion of Ge diffuses into the absorber and combines with Se to form Ge–Se liquid fluxes, promoting nucleation and grain growth, resulting in flatter CZTSSe films with fewer pinholes. This can significantly reduce the defect density, band tail, and promote quasi Fermi-level splitting through the relatively higher hole concentration. At the same time, another part of Ge diffuses into the $MoSe_2$ layer, increasing the work function of $MoSe_2$, which may act as an electronic barrier at the back interface and inhibit the recombination of photogenerated carriers. As a result, the device achieved a V_{OC}/V_{OC}^{SQ} of 63.1%, which is the lowest V_{OC} loss of any Ge-doped CZTSSe solar cells reported.

2.2 Front interface

2.2.1 Recent problems at the front interface. In CZTSSe thin-film solar cells, the n-type layer of the p–n junction usually consists of CdS prepared by a chemical bath deposition (CBD) layer and ZnO prepared by sputtering. The Cd/CZTSSe interface plays a vital role in carrier separation. However, severe non-radiative recombination at the CdS/CZTSSe interface is another important factor leading to a high V_{OC} deficit.[91] According to experimental and theoretical calculations, there are two types of energy-band alignment at the heterogeneous junction. Fig. 5a shows the spike-type (type I) alignment, in

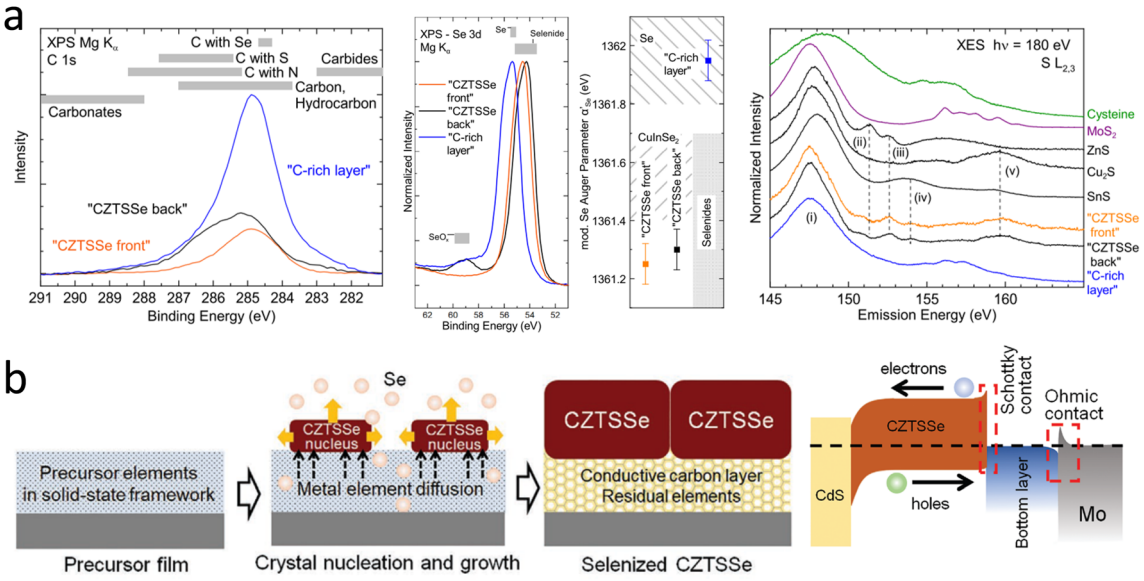

Fig. 3 (a) C 1s XPS, Se 3d XPS, and XES spectra of the investigated samples.[64] Reproduced with permission from ref. 64. (b) Schematic diagrams of the TGA-ammonia method and the energy-band structure of the cell.[63] Reproduced with permission from ref. 63.

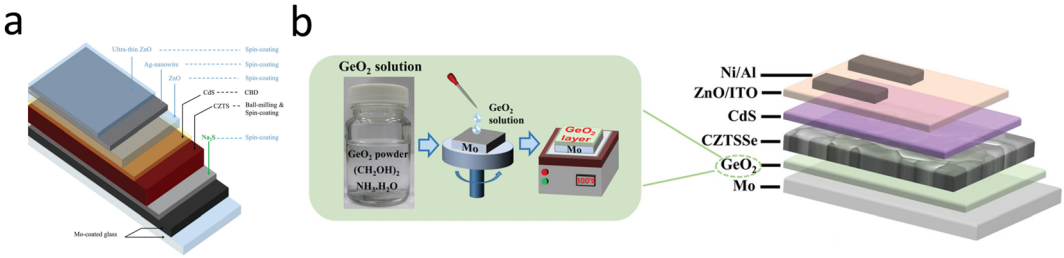

Fig. 4 (a) Schematic diagram of CZTS solar cells.[43] Reproduced with permission from ref. 43. (b) Schematic diagram of CZTSSe devices containing GeO_2 layers.[46] Reproduced with permission from ref. 46.

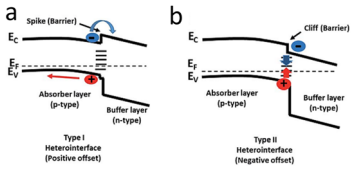

Fig. 5 Types of heterojunction interface alignments for the absorber and buffer layers: (a) type I (spike), (b) type II (cliff).[33] Reproduced with permission from ref. 33.

which the conduction band offset (CBO) value is greater than 0 eV, and there is a specific photogenerated electron barrier. If the value of the CBO is above 0.4 eV, it will significantly impact the photogenerated current. The other type is called the cliff-type (type II) energy-band alignment, in which the CBO is negative, facilitating charge recombination, and reducing the V_{OC}, as shown in Fig. 5b. Therefore, a spike type with a CBO below 0.4 eV is preferred for high-performance CZTSSe solar cells. This design is also adopted by highly efficient GIGS solar cells, where the energy-band alignment is the spike type with a CBO less than 0.4 eV.[10,39] In kesterite solar cells, the band alignment at CZTSSe/CdS is changed as a function of S/(S + Se) owing to the different conduction band offset (CBO). The CBO of CZTS/CdS is usually considered as a cliff, whereby with increasing the Se concentration in CZTSSe, the downward shift of the CBM leads to this spike-like alignment.[32,92–94]

In CZTSSe, the surface could not form the n-type due to the dissolution of Zn^{2+} on its surface by the ammonia ($NH_3 \cdot H_2O$) in the solution during the deposition of CdS to form Zn vacancies, and the occupation of Zn vacancies (not Cu vacancies) by Cd^{2+}, resulting in lattice strain due to the significant difference in the radii of the Cd^{2+} and Zn^{2+} ions.[15,27,32,95] It was found experimentally that the surface of CZTSSe was indeed a p-type (no type inversion),[3] in agreement with the theoretical analysis. Since the maximum V_{OC} under illumination (in the band conditions shown in Fig. 6) was equal to the band bending of the absorber layer in the dark, Fermi-level pinning caused by the surface Cu_{Zn} defects (and hence no type inversion) led to a substantial deficit in V_{OC}.[95] This inability of the surface to achieve p–n inversion hindered the V_{OC}. In contrast, type-reversal band bending was observed in the CIGS solar cells, which gave them a much higher V_{OC} than the CZTSSe solar cells, as shown in Fig. 6c and d.[95–97] Therefore, if the intention is to overcome the V_{OC} deficit in CZTSSe solar cells, it is crucial to suppress the formation of Cu_{Zn} defects and make the type conversion at the p–n junction interface possible.

Researchers have done much work on heterojunctions to solve energy-band-alignment mismatches and interfacial defects.[24,39] The optimization of heterojunctions can be split into three main areas: introduction of ultrathin passivation layers,[98–100] alternative buffer layers,[101–105] and annealing of heterojunctions.[32,40,106–109] An ultrathin passivation layer alters the local chemistry of the surface and reduces defect-assisted interfacial recombination.[100] Alternative buffer layers can replace conventional CdS buffer layers with tunable band gaps to create a favorable band alignment.[11,103] Furthermore, heat treatment after deposition of the CdS buffer layer can significantly improve the performance of the heterojunction due to the formation of interlayers and the compensation of defects by diffusion between the elements.[32,108]

2.2.2 Passivation layers. The role of interfacial passivation layers in CZTSSe has been of great interest to researchers because of the ability of interfacial passivation to reduce non-radiative recombination at the CZTSSe/CdS interface. One approach to passivation defect-assisted interfacial

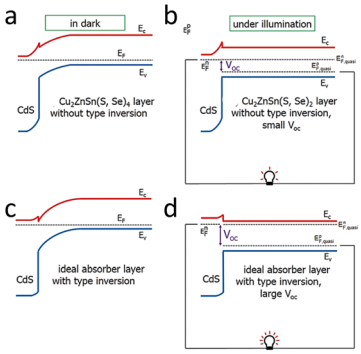

Fig. 6 Band diagrams of solar cells in the dark (left) and under illumination (right). (a) CdS/CZTSSe solar cells without type inversion (Fermi level near the interface pinned to the middle of the band gap) and with a slight band bending in the absorber layer, and (b) CdS/CZTSSe solar cells with negligible V_{OC} under flat band conditions. (c) Ideal absorber layer with type reversal (Fermi level near the interface close to the conduction band), considerable band bending, and (d) perfect absorber layer with significant V_{OC} under in-band flat conditions.[95] Reproduced with permission from ref. 95.

recombination is by inserting an ultrathin dielectric layer.[98–100] To date, different materials (*e.g.*, TiO_2,[110] SnO_2,[111] Al_2O_3,[98–100] and In_2S_3 (ref. 112)) have been developed as passivation layers for CZTSSe.[33] The primary role of most passivation layers is to passivate the interface defects and optimize the band alignment and thus reduce the interface recombination.[100,111,113]

Wu *et al.* reported that ALD-coated TiO_2 films on CZTSSe photovoltaic devices could reduce interfacial recombination and improve device performance, as shown in Fig. 7a. After ALD deposition, the V_{OC} of the device was increased from 397 mV to 433 mV.[110] These results clearly illustrate the surface passivation effect of the ALD layer in CZTSSe devices and showed that adding an ALD passivation layer is a potential way to improve the V_{OC}. Subsequently, Sun *et al.*[111] used the successive ionic layer adsorption and reaction (SILAR) method to deposit an ultrathin SnO_2 interlayer, which was introduced into the heterogeneous interface between a p-type CZTS absorber and an n-type CdS buffer for passivation of the interfacial defects in CZTSSe thin-film solar cells, and the specific details are shown in Fig. 7b. The V_{OC} values of CZTS with and without the SnO_2 interlayer were 657 mV and 638 mV, and the FF values were 62.8% and 52.4%, respectively. The mitigation of the V_{OC} deficit and improvement in FF were believed to result from the combined effects of CZTS/CdS heterogeneous interfacial passivation, shunt blocking, and band alignment.

Many researchers later considered the conformal coating of Al_2O_3 grown on CZTSSe by ALD as an effective method to reduce interfacial recombination. Some also found that inserting a thin Al_2O_3 layer between CdS and TCO could also work as armor shield to prevent damage to CdS during TCO fabrication.[98–100] Xiaojing Hao's group found that applying a complete ALD–Al_2O_3 cycle and trimethyl aluminum (TMA) exposure resulted in a significant increase in V_{OC} and linked this to the properties of the CZTS interface. Both processes favored the formation of a thicker Cu-deficient nanolayer with higher concentrations of Na and O, forming a homogeneous passivation layer on the CZTS surface. The nanolayer reduced potential local fluctuations at the band edge, widened the electric band gap, and suppressed recombination at the heterojunction interface, thereby improving the V_{OC} and device performance, as shown in Fig. 7c. The ability of the nanolayer to alter the atomic composition of the near-surface region makes it a universal approach for surface passivation.[100]

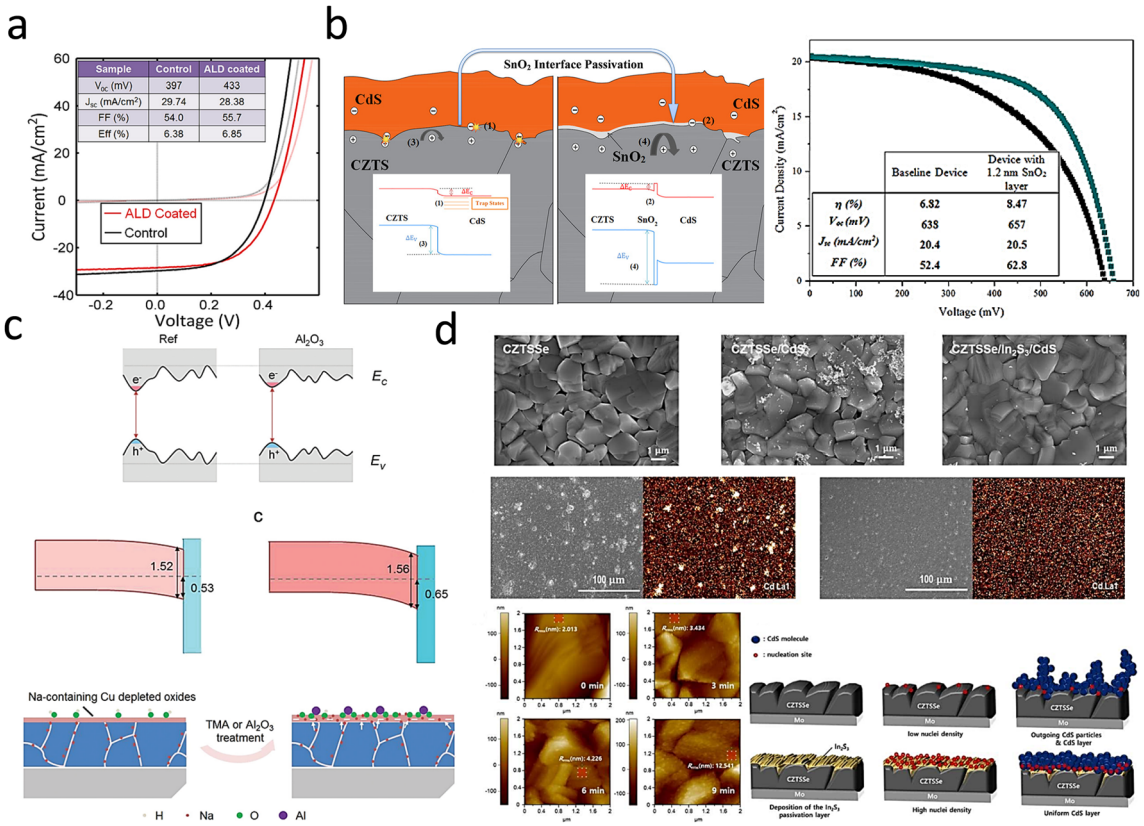

Fig. 7 (a) *J*–*V* curves of an ALD–TiO_2-treated CZTSSe cell.[110] Reproduced with permission from ref. 110. (b) Schematic band diagrams of the CZTS/SnO_2/CdS heterojunctions and *J*–*V* curves.[111] Reproduced with permission from ref. 111. (c) Schematic band gap fluctuation in the electronic structures of CZTS with and without Al_2O_3 treatment and mechanism illustration of the CZTS absorber surface modification when exposed to ALD–Al_2O_3 treatment.[100] Reproduced with permission from ref. 100. (d) SEM top-view images of CZTSSe/CdS and CZTSSe/In_2S_3/CdS films and EDS mapping images, surface AFM images of bare CZTSSe films (0 min) and CZTSSe/In_2S_3 films for different In_2S_3 deposition times (3, 6, 9 min) and schematic representation of the other morphological evolution mechanisms according to the presence of In_2S_3 layers.[112] Reproduced with permission from ref. 112.

Recently, an In_2S_3 passivation layer was used with the CZTSSe/CdS interface to improve the front interface roughness and reduce interfacial recombination, and it was demonstrated that this method could effectively control the surface morphology and defect density of CZTSSe thin-film solar cells.[112] The presence of the In_2S_3 layer led to an homogeneous growth of CdS without macroscopic CdS agglomeration (*i.e.*, a reduced roughness of the full device), thereby improving the quality of the heterojunction (as shown in Fig. 7d). The In_2S_3 passivation layers contributed to the reduction of non-radiative recombination by reducing the deep energy level defects and increasing the minority carrier lifetimes. Similarly, the improved interfacial morphology and photovoltaic performance provided by the thin In_2S_3 passivation layers were very promising for both CZTSSe single solar cells and tandem solar cells, as the relatively rough surface and poor photovoltaic performance are currently the main obstacles to achieving efficient CZTSSe-based tandem solar cells.

2.2.3 Alternative buffer layers. CdS is the most commonly used n-type buffer layer in laboratory and module production because of its simple and cost-effective synthesis.[91,114] However, its application is limited due to its toxicity, generation of hazardous waste after deposition, and low J_{SC} due to parasitic losses in the short-wavelength range.[100,115] On the one hand, the conduction band offset between CdS and CZTSSe is an essential cause of the voltage deficit,[116,117] while on the other hand, the lattice mismatch at the interface between CZTS and CdS is ~7% (or for CIGS and CdS, it is ~1.5%),[118,119] and high area density interface defects can therefore be anticipated at the CZTS/CdS interface, thus increasing interfacial Shockley–Read–Hall recombination and decreasing the VOC of the device.[119] In addition, the relatively low band gap of CdS (E_g = 2.4–2.5 eV) leads to a significant loss of light absorption, reducing the solar cells' J_{SC}. To overcome these problems, alternative buffer layers have been proposed,[11,13,102,104,120] and some representative works reporting alternative buffer layers of CZTSSe are presented in Table 2.

Non-toxic, environmentally friendly wide-band-gap n-type semiconductors with suitable CBO are favorable for alternative buffer layers.[126] Among the many alternative buffer layers, ZnSnO is a shining star due to its unique advantages. The band gap can be adjusted by adjusting the Zn/Sn ratio; the structure of the interfacial energy band is shown in Fig. 8a.[103] The increased efficiency of ZnSnO is not only due to the excellent energy-band alignment but also to the formation of an ultrathin Zn(O,S) tunneling layer between CZTS/ZnSnO, which acts as an effective cavity barrier at the interface.[13] Atomic layer deposition (ALD) is a widely adopted method for depositing ZnSnO buffers. The properties of the ZnSnO buffer layer can be tuned by adjusting the deposition temperature and the metal stoichiometry ratio, as shown in Fig. 8b.[100,103] The structure of a CZTS solar cells device with a ZnSnO buffer layer is shown in Fig. 8c. Wang *et al.* introduced an additional In_2S_3 buffer layer to modify the properties of the Zn(O,S) and CZTSSe layers by a post-annealing treatment. The increased carrier concentration in the Zn(O,S) and CZTSSe layers facilitated carrier separation and increased the V_{OC}. The results showed that the efficiency of CZTSSe solar cells was increased by 24% after the annealing and etching treatment. Simulation and experimental results showed that the significant band shift of the In_2S_3 layer and the defect energy level of the Zn(O,S) layer were the main characteristics limiting the FF and efficiency of these CZTSSe devices, as shown in Fig. 8d.[121] The In_2S_3 material is an effective alternative to CdS buffer layers due to its non-toxic and suitable indirect band gap (E_g = 2.1 eV). The CZTS/In_2S_3 heterojunction with a positive CBO of 0.11 eV facilitated carrier separation and transport at the interface, as shown in Fig. 8e. However, the CBO of CZTSSe/In_2S_3 was more significant than 0.4 eV, which is not conducive to carrier transport, so it has been less studied as a buffer layer.[101]

2.2.4 Annealing of the heterojunction. In recent years, heterojunction heat treatment has been widely reported to improve the photovoltaic performance of CZTSSe solar cells. Improved heterojunction interfaces are mainly attributed to ordered–disordered jumps in the bulk and interdiffusion within the interface region. Research into low-temperature post-annealing treatments has confirmed changes in the degree of ordered disorder where harmful defects with high formation

Table 2 Representative works reporting alternative buffer layers of CZTSSe

Buffer layer	Absorber	Deposition method	Thickness (nm)	V_{OC} (mV)	J_{SC} (mA cm^{-2})	FF (%)	PCE (%)	References
ZnSnO	CZTS	ALD	10	720	20.5	63.5	9.3	13
	CZTS	ALD	10	736	21.0	65.8	10.2	100
	CZTS	ALD	56	746	19.1	68.0	9.7	11
	CZTS	RF sputtering	50	721	14.0	51.4	5.2	115
	CZTSSe	RF sputtering	~20	445	36.4	69.3	11.2	103
ZnCdS	CZTS	SILAR	70	747	19.5	63.2	9.2	102
	CZTS	SILAR	70	735	20.1	62.5	9.3	105
	CZTS	CBD	60	683	22.2	66.3	10.1	104
Zn(O,S)	CZTSSe	CBD	—	346	34.8	47.8	5.8	121
	CZTSSe	ALD	20	496	35.6	56.0	9.8	122
ZnS	CZTSSe	CBD	30–50	596	15.4	49.1	4.5	123
	CZTSSe	CBD	70	309	23.5	54.0	3.8	124
In_2S_3	CZTS	CBD	90	585	17.0	45.0	4.5	101
	CZTS	CBD	60	738	17.6	55.5	7.2	125

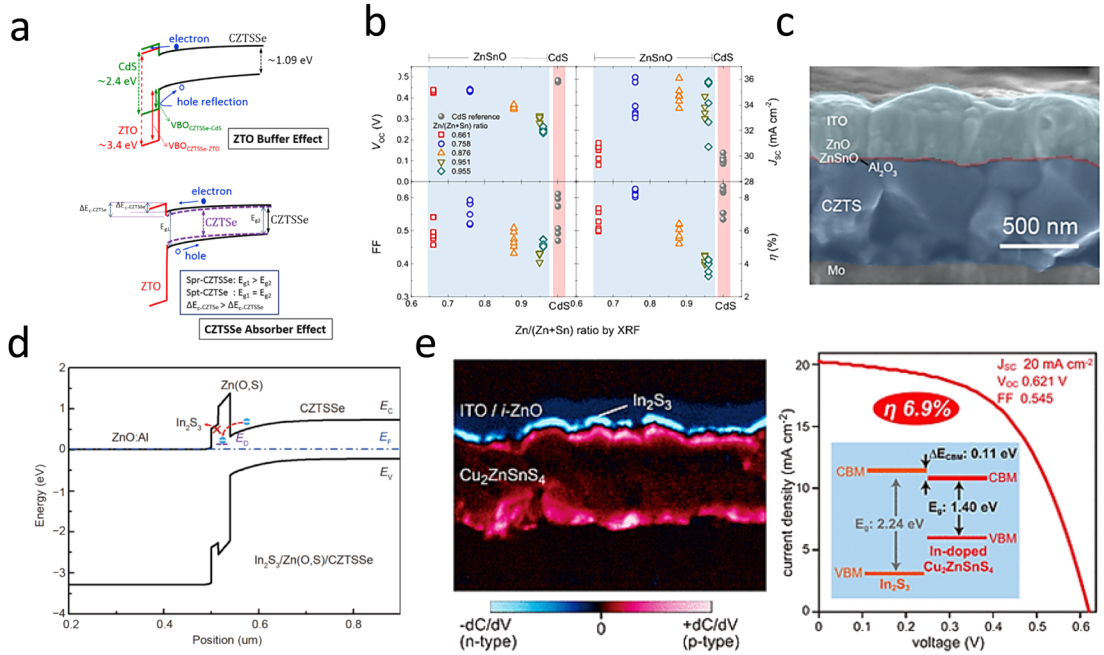

Fig. 8 (a) Schematic diagram of the energy-band structure between CZTSSe and ZnSnO.[103] Reproduced with permission from ref. 103. (b) CZTSSe/CdS and CZTSSe/ZnSnO device performance with different Sn, Zn ratios.[120] Reproduced with permission from ref. 120. (c) SEM cross-sectional image of Cd-free CZTS solar cells with an Al_2O_3 passivation layer inserted between CZTS and ZnSnO.[100] Reproduced with permission from ref. 100. (d) Schematic diagram of the band alignment of the In_2S_3/Zn(O,S)/CZTSSe interface for the device.[121] Reproduced with permission from ref. 121. (e) Cross-sectional SCM images of solar cells based on In_2S_3/Cu_2ZnSnS_4 and *J*–*V* curves.[101] Reproduced with permission from ref. 101.

energies can be mitigated, while defect clusters with low formation energies cannot. Also, some representative works reporting annealing of the heterojunctions of CZTSSe are presented in Table 3.

Severe non-radiative recombination within the heterojunction region is a major cause of a limited voltage output and overall performance. A certified CZTS solar cell with an efficiency of 11.0% was reported, where heterojunction recombination was reduced by heat treatment, which promoted elemental interdiffusion and directly induced Cd atoms to occupy Zn/Cu lattice sites, promoting local Cu deficiency within the heterojunction region of Na accumulation. As a result, new phases were formed near the heterogeneous interface, obtaining a more favorable conduction band alignment and contributing to a reduction in non-radiative recombination, as shown in Fig. 9a.[108] Heterojunction annealing is not only effective in the CZTS system but also plays a great role in the CZTSSe system, where it enables a custom band alignment between p–n junctions to improve the electron transport and reduce carrier recombination. This

Table 3 Representative works reporting annealing of the heterojunction of CZTSSe

	Annealing							PCE (%)		
Absorber	Temp. (°C)	Time (min)	Step	Atmosphere	V_{OC} (mV)	J_{SC} (mA cm^{-1})	FF (%)	Before	After	References
CZTSSe	220	3	After cell	Air	358	27.9	32.9	3.7	3.3	107
	270	3			424	31.7	59.7	4.4	8.0	
	320	3			400	28.1	38.6	4.3	4.3	
CZTS	270	10	After CdS	N_2	731	21.7	69.3	7.8	11.0	108
CZTSSe	200	2	After CdS	Vacuum	522	33.3	71.5	10.9	12.4	109
	200	20			513	35.1	72.5	10.9	13.0	
CZTSSe	90	60	After CdS	N_2	476	36.7	63.0	10.4	11.1	94
	210	1			472	36.7	57.0	10.4	10.0	
	90–210	60–1			487	37.0	67.0	10.4	12.1	
CZTSSe	250	5	After CdS	N_2	362	27.6	45.6	7.6	4.6	127
	300	5			350	25.9	32.1	7.6	2.9	
CZTSSe	150	90	During sputtering	Ar	484	37.8	66.9	8.4	12.3	40
CZTSSe	110	720	After CdS	N_2	532	34.2	73.4	11.1	13.4	32

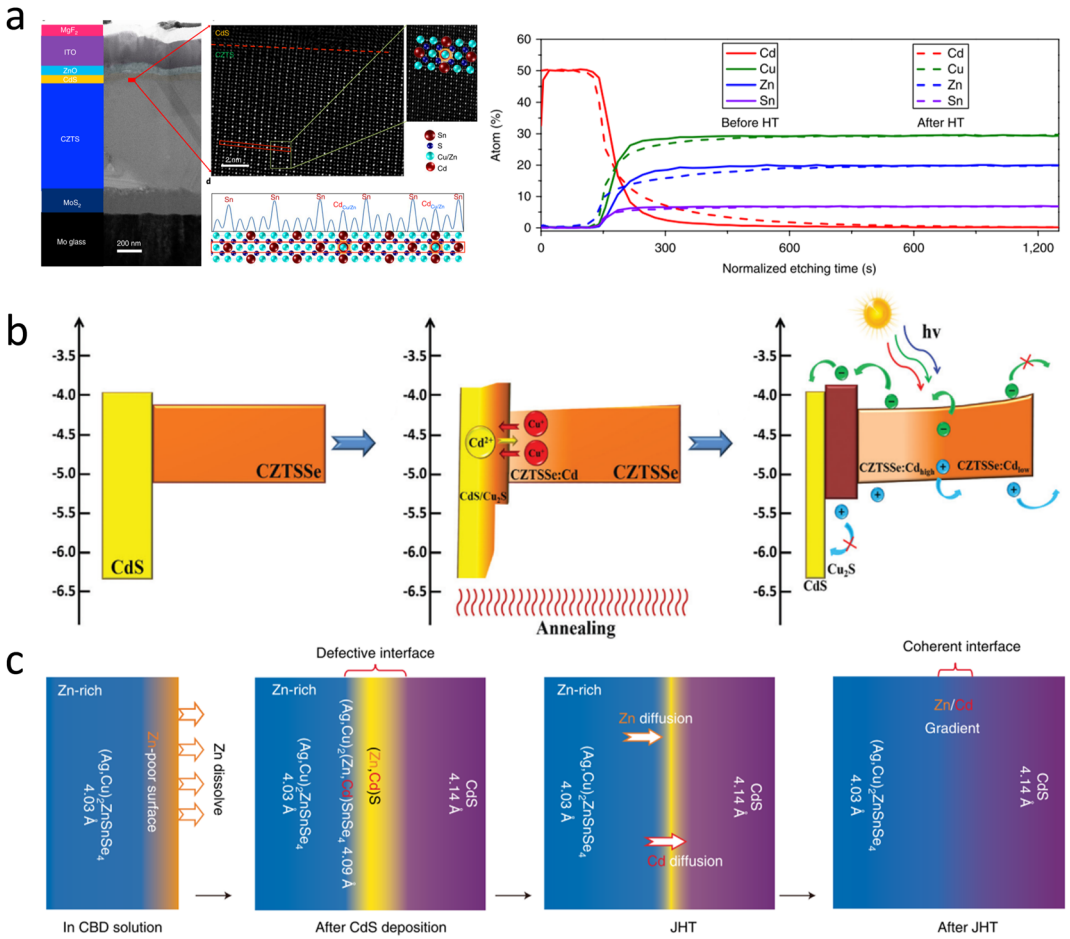

Fig. 9 (a) TEM cross-section of a CZTS device using the HT process, with the corresponding device structure shown on the left.[108] Reproduced with permission from ref. 108. (b) Schematic of the energy-band structure and the diffusion of Cu^+ and Cd^{2+} ions during heterojunction annealing.[40] Reproduced with permission from ref. 40. (c) Schematic of the diffusion of the ions during heterojunction annealing.[32] Reproduced with permission from ref. 32.

annealing strategy promotes a solid-state ion-exchange reaction between Cu^+ and Cd^{2+} at the heterojunction interface. As a result, p-type Cu_2S is formed at the interface, and CZTSSe is gradient doped by Cd, resulting in the desired band structure, as shown in Fig. 9b. The tailored band alignment between the p–n junctions improves electron transport and reduces carrier recombination. Recently, researchers have made new progress in heterojunction annealing.[32] The PCE of a cell obtained by low-temperature heat treatment of the silver alloy ACZTSSe/CdS heterojunction and various characterizations showed that the improvement in cell performance was mainly due to the reduction in defect concentration at the heterojunction interface. The low-temperature heat treatment induced the migration and rearrangement of elements near the heterojunction interface, including the reverse mixing of Cd^{2+} and Zn^{2+} ions at the interface and the diffusion of Zn^{2+} from the bulk phase to the absorber layer interface, achieving a gradient distribution of Zn and Cd elements near the interface and promoting the formation of the epitaxial ACZTSSe/CdS interface, as shown in Fig. 9c. This work set a new world record efficiency (13.0%) for ACZTSSe solar cells.

Heterojunction annealing is a major tool for improving the efficiency of CZTSSe solar cells. With the advancement of heterojunction annealing research, it is believed that heterojunction annealing can facilitate the diffusion of Cd, Zn, and Cu elements in the heterojunction region and help solve the lattice and energy band mismatch problems.

3. Summary and future perspectives

Due to its unique advantages, CZTSSe is regarded as a candidate with good potential for next-generation photovoltaic devices. Currently, the record efficiency of CZTSSe is still much lower than the S–Q limit efficiency, mainly caused by the excessive V_{OC} deficit. The interface problem accounts for a large proportion of the problem of low efficiency. This review systematically listed and analyzed the interface engineering modification strategies, including the back interface and front interface, and introduced the latest research progress in related fields.

More efforts are needed on interface engineering to improve the performance of CZTSSe solar cells further. Based on the current status, we make the following outlook: in terms of back-

interface engineering, wide-band gap blocking layers create additional R_S, which affects the solar cell parameters, especially the FF. Future work should focus on developing blocking layers with good chemical durability to prevent side reactions at the back interface. For the front interface, more efforts are needed to regulate the surface lattice mismatch, thus decreasing the trap densities and facilitating energy level matching. Controlling elemental interdiffusion in CZTSSe/CdS solar cells by heterojunction engineering is a powerful way to improve the interfacial properties. We believe that with the efforts of researchers, the current problems hindering the development of CZTSSe solar cells will be solved and will make it a shining star in the photovoltaic industry.

Author contributions

All authors researched data for the article and contributed to the content discussion. Yimeng Li wrote the article, Hao Wei, Xiao Wang, and Changcheng Cui participated in literature research and collection, and Zhipeng Shao, Shuping Pang and Guanglei Cui edited and reviewed the article prior to submission.

Conflicts of interest

The authors declare no competing interest.

Acknowledgements

This study is financially supported by the Major Basic Research Projects of the Shandong Natural Science Foundation (Grant No. ZR2021ZD25), the National Natural Science Foundation of China (Grant No. 22279154, 52272255), and Shandong Energy Institute (SEI I202129).

References

1 T. D. Lee and A. U. Ebong, *Renewable Sustainable Energy Rev.*, 2017, **70**, 1286–1297.
2 D. Shin, T. Zhu, X. Huang, O. Gunawan, V. Blum and D. B. Mitzi, *Adv. Mater.*, 2017, **29**, 1606945.
3 Y. Sun, P. Qiu, W. Yu, J. Li, H. Guo, L. Wu, H. Luo, R. Meng, Y. Zhang and S. F. Liu, *Adv. Mater.*, 2021, **33**, 2104330.
4 S. Liu, Y. Guan, Y. Sheng, Y. Hu, Y. Rong, A. Mei and H. Han, *Adv. Energy Mater.*, 2019, **10**, 1902492.
5 S. Wang, L. Huang, Z. Ye, L. Zhong, G. Chen, J. Li and X. Xiao, *J. Mater. Chem. A*, 2021, **9**, 25522–25530.
6 O. Stroyuk, A. Raevskaya and N. Gaponik, *Chem. Soc. Rev.*, 2018, **47**, 5354–5422.
7 K.-J. Yang, D.-H. Son, S.-J. Sung, J.-H. Sim, Y.-I. Kim, S.-N. Park, D.-H. Jeon, J. Kim, D.-K. Hwang, C.-W. Jeon, D. Nam, H. Cheong, J.-K. Kang and D.-H. Kim, *J. Mater. Chem. A*, 2016, **4**, 10151–10158.
8 H. Xu, S. Ge, W. Yang, S. N. Khan, Y. Huang, Y. Mai, E. Gu, X. Lin and G. Yang, *J. Mater. Chem. A*, 2021, **9**, 25062–25072.
9 A. Chirila, P. Reinhard, F. Pianezzi, P. Bloesch, A. R. Uhl, C. Fella, L. Kranz, D. Keller, C. Gretener, H. Hagendorfer, D. Jaeger, R. Erni, S. Nishiwaki, S. Buecheler and A. N. Tiwari, *Nat. Mater.*, 2013, **12**, 1107–1111.
10 J.-f. Han, C. Liao, L.-m. Cha, T. Jiang, H.-m. Xie, K. Zhao and M. P. Besland, *J. Phys. Chem. Solids*, 2014, **75**, 1279–1283.
11 J. K. Larsen, F. Larsson, T. Törndahl, N. Saini, L. Riekehr, Y. Ren, A. Biswal, D. Hauschild, L. Weinhardt, C. Heske and C. Platzer-Björkman, *Adv. Energy Mater.*, 2019, **9**, 1900439.
12 D. Shin, B. Saparov and D. B. Mitzi, *Adv. Energy Mater.*, 2017, **7**, 1602366.
13 X. Cui, K. Sun, J. Huang, C.-Y. Lee, C. Yan, H. Sun, Y. Zhang, F. Liu, M. A. Hossain, Y. Zakaria, L. H. Wong, M. Green, B. Hoex and X. Hao, *Chem. Mater.*, 2018, **30**, 7860–7871.
14 T. Zhu, W. P. Huhn, G. C. Wessler, D. Shin, B. Saparov, D. B. Mitzi and V. Blum, *Chem. Mater.*, 2017, **29**, 7868–7879.
15 K. Pal, P. Singh, A. Bhaduri and K. B. Thapa, *Sol. Energy Mater. Sol. Cells*, 2019, **196**, 138–156.
16 Q. Tian and S. Liu, *J. Mater. Chem. A*, 2020, **8**, 24920–24942.
17 H. Katagiri, K. Jimbo, W. S. Maw, K. Oishi, M. Yamazaki, H. Araki and A. Takeuchi, *Thin Solid Films*, 2009, **517**, 2455–2460.
18 M. Kumar, A. Dubey, N. Adhikari, S. Venkatesan and Q. Qiao, *Energy Environ. Sci.*, 2015, **8**, 3134–3159.
19 D. B. Mitzi, O. Gunawan, T. K. Todorov, K. Wang and S. Guha, *Sol. Energy Mater. Sol. Cells*, 2011, **95**, 1421–1436.
20 A. Polizzotti, I. L. Repins, R. Noufi, S.-H. Wei and D. B. Mitzi, *Energy Environ. Sci.*, 2013, **6**, 3171–3182.
21 S. Chen, A. Walsh, X. G. Gong and S. H. Wei, *Adv. Mater.*, 2013, **25**, 1522–1539.
22 C. Platzer-Björkman, N. Barreau, M. Bär, L. Choubrac, L. Grenet, J. Heo, T. Kubart, A. Mittiga, Y. Sanchez, J. Scragg, S. Sinha and M. Valentini, *J. Phys.: Energy*, 2019, **1**, 044005.
23 V. Karade, A. Lokhande, P. Babar, M. G. Gang, M. Suryawanshi, P. Patil and J. H. Kim, *Sol. Energy Mater. Sol. Cells*, 2019, **200**, 109911.
24 M. He, K. Sun, M. P. Suryawanshi, J. Li and X. Hao, *J. Energy Chem.*, 2021, **60**, 1–8.
25 J. Li, J. Huang, F. Ma, H. Sun, J. Cong, K. Privat, R. F. Webster, S. Cheong, Y. Yao, R. L. Chin, X. Yuan, M. He, K. Sun, H. Li, Y. Mai, Z. Hameiri, N. J. Ekins-Daukes, R. D. Tilley, T. Unold, M. A. Green and X. Hao, *Nat. Energy*, 2022, **7**, 754–764.
26 H. Guo, G. Wang, R. Meng, Y. Sun, S. Wang, S. Zhang, J. Wu, L. Wu, G. Liang, H. Li and Y. Zhang, *J. Mater. Chem. A*, 2020, **8**, 22065–22074.
27 F. Liu, S. Wu, Y. Zhang, X. Hao and L. Ding, *Sci. Bull.*, 2020, **65**, 698–701.
28 M. He, C. Yan, J. Li, M. P. Suryawanshi, J. Kim, M. A. Green and X. Hao, *Adv. Sci.*, 2021, **8**, 2004313.
29 S. Hadke, M. Huang, C. Chen, Y. F. Tay, S. Chen, J. Tang and L. Wong, *Chem. Rev.*, 2021, **122**, 10170–10265.
30 Y. Lei, Y. Li and Z. Jin, *Energy Rev.*, 2022, **1**, 100003.
31 F. Liu, Q. Zeng, J. Li, X. Hao, A. Ho-Baillie, J. Tang and M. A. Green, *Mater. Today*, 2020, **41**, 120–142.

32 Y. Gong, Q. Zhu, B. Li, S. Wang, B. Duan, L. Lou, C. Xiang, E. Jedlicka, R. Giridharagopal, Y. Zhou, Q. Dai, W. Yan, S. Chen, Q. Meng and H. Xin, *Nat. Energy*, 2022, **7**, 966–977.
33 Nisika, K. Kaur and M. Kumar, *J. Mater. Chem. A*, 2020, **8**, 21547–21584.
34 Z. Zhang, L. Yao, Y. Zhang, J. Ao, J. Bi, S. Gao, Q. Gao, M. J. Jeng, G. Sun, Z. Zhou, Q. He and Y. Sun, *Adv. Sci.*, 2018, **5**, 1700645.
35 A. Wang, M. He, M. A. Green, K. Sun and X. Hao, *Adv. Energy Mater.*, 2022, **13**, 2203046.
36 K. Sun, J. Huang, J. Li, C. Yan and X. Hao, *Sci. China: Phys., Mech. Astron.*, 2022, **66**, 217302.
37 J. Zhou, X. Xu, B. Duan, H. Wu, J. Shi, Y. Luo, D. Li and Q. Meng, *Nano Energy*, 2021, **89**, 106405.
38 Z. Shen, S. Wang, Y. Liu, Y. Sun, J. Wu, H. Guo, K. Zhang, S. Zhang, F. Liu and Y. Zhang, *J. Energy Chem.*, 2021, **62**, 637–644.
39 A. Crovetto and O. Hansen, *Sol. Energy Mater. Sol. Cells*, 2017, **169**, 177–194.
40 H. Guo, R. Meng, G. Wang, S. Wang, L. Wu, J. Li, Z. Wang, J. Dong, X. Hao and Y. Zhang, *Energy Environ. Sci.*, 2022, **15**, 693–704.
41 E. Ojeda-Durán, K. Monfil-Leyva, J. Andrade-Arvizu, I. Becerril-Romero, Y. Sánchez, R. Fonoll-Rubio, M. Guc, Z. J. Li-Kao, J. A. Luna-López and E. Saucedo, *J. Mater. Chem. C*, 2021, **9**, 5356–5361.
42 K. Yin, X. Xu, M. Wang, J. Zhou, B. Duan, J. Shi, D. Li, H. Wu, Y. Luo and Q. Meng, *J. Mater. Chem. A*, 2022, **10**, 779–788.
43 Y. Gu, H. Shen, C. Ye, X. Dai, Q. Cui, J. Li, F. Hao, X. Hao and H. Lin, *Adv. Funct. Mater.*, 2018, **28**, 1703369.
44 J. J. Scragg, T. Kubart, J. T. Wätjen, T. Ericson, M. K. Linnarsson and C. Platzer-Björkman, *Chem. Mater.*, 2013, **25**, 3162–3171.
45 H.-J. Chen, S.-W. Fu, S.-H. Wu, T.-C. Tsai, H.-T. Wu, C.-F. Shih and P. Gouma, *J. Am. Ceram. Soc.*, 2016, **99**, 1808–1814.
46 J. Wang, J. Zhou, X. Xu, F. Meng, C. Xiang, L. Lou, K. Yin, B. Duan, H. Wu, J. Shi, Y. Luo, D. Li, H. Xin and Q. Meng, *Adv. Mater.*, 2022, **34**, 2202858.
47 A. Cabas-Vidani, L. Choubrac, J. A. Marquez, T. Unold, M. Maiberg, R. Scheer, H. Li, K. Leifer, R. Pauer, E. Gilshtein, A. N. Tiwari and Y. E. Romanyuk, *ACS Appl. Mater. Interfaces*, 2021, **13**, 19487–19496.
48 B. Shin, N. A. Bojarczuk and S. Guha, *Appl. Phys. Lett.*, 2013, **102**, 091907.
49 X. Yin, C. Tang, L. Sun, Z. Shen and H. Gong, *Chem. Mater.*, 2014, **26**, 2005–2014.
50 G. Brammertz, M. Buffière, S. Oueslati, H. ElAnzeery, K. Ben Messaoud, S. Sahayaraj, C. Köble, M. Meuris and J. Poortmans, *Appl. Phys. Lett.*, 2013, **103**, 163904.
51 J. J. Scragg, P. J. Dale, D. Colombara and L. M. Peter, *ChemPhysChem*, 2012, **13**, 3035–3046.
52 W. Wang, G. Chen, H. Cai, B. Chen, L. Yao, M. Yang, S. Chen and Z. Huang, *J. Mater. Chem. A*, 2018, **6**, 2995–3004.
53 D. Cozza, C. M. Ruiz, D. Duche, J. J. Simon and L. Escoubas, *IEEE J. Photovoltaics*, 2016, **6**, 1292–1297.
54 J. Li, Y. Zhang, W. Zhao, D. Nam, H. Cheong, L. Wu, Z. Zhou and Y. Sun, *Adv. Energy Mater.*, 2015, **5**, 1402178.
55 W. Li, X. Han, Y. Zhao and S. Yang, *J. Mater. Sci.: Mater. Electron.*, 2016, **27**, 11188–11191.
56 S. W. Shin, K. V. Gurav, C. W. Hong, J. Gwak, H. R. Choi, S. A. Vanalakar, J. H. Yun, J. Y. Lee, J. H. Moon and J. H. Kim, *Sol. Energy Mater. Sol. Cells*, 2015, **143**, 480–487.
57 G. K. Dalapati, S. Zhuk, S. Masudy-Panah, A. Kushwaha, H. L. Seng, V. Chellappan, V. Suresh, Z. Su, S. K. Batabyal, C. C. Tan, A. Guchhait, L. H. Wong, T. K. S. Wong and S. Tripathy, *Sci. Rep.*, 2017, **7**, 1350.
58 X. Lu, B. Xu, X. Qin, Y. Chen, P. Yang, J. Chu and L. Sun, *ACS Appl. Mater. Interfaces*, 2020, **12**, 58060–58071.
59 S.-Y. Kim, D.-H. Son, Y.-I. Kim, S.-H. Kim, S. Kim, K. Ahn, S.-J. Sung, D.-K. Hwang, K.-J. Yang, J.-K. Kang and D.-H. Kim, *Nano Energy*, 2019, **59**, 399–411.
60 Z. Wei, C. M. Fung, A. Pockett, T. O. Dunlop, J. D. McGettrick, P. J. Heard, O. J. Guy, M. J. Carnie, J. H. Sullivan and T. M. Watson, *ACS Appl. Energy Mater.*, 2018, **1**, 2749–2757.
61 T. Schnabel and E. Ahlswede, *Sol. Energy Mater. Sol. Cells*, 2017, **159**, 290–295.
62 H. Guo, C. Ma, K. Zhang, X. Jia, X. Wang, N. Yuan and J. Ding, *Sol. Energy Mater. Sol. Cells*, 2018, **175**, 20–28.
63 X. Xu, L. Guo, J. Zhou, B. Duan, D. Li, J. Shi, H. Wu, Y. Luo and Q. Meng, *Adv. Energy Mater.*, 2021, **11**, 2102298.
64 D. Hauschild, S. J. Wachs, W. Kogler, L. Seitz, J. Carter, T. Schnabel, B. Krause, M. Blum, W. Yang, E. Ahlswede, C. Heske and L. Weinhardt, *IEEE J. Photovoltaics*, 2021, **11**, 658–663.
65 W. Kogler, T. Schnabel, E. Ahlswede and M. Powalla, *Sol. Energy Mater. Sol. Cells*, 2019, **200**, 109959.
66 Y. Zhao, Z. Yu, J. Hu, Z. Zheng, H. Ma, K. Sun, X. Hao, G. Liang, P. Fan, X. Zhang and Z. Su, *J. Energy Chem.*, 2022, **75**, 321–329.
67 F. Liu, J. Huang, K. Sun, C. Yan, Y. Shen, J. Park, A. Pu, F. Zhou, X. Liu, J. A. Stride, M. A. Green and X. Hao, *NPG Asia Mater.*, 2017, **9**, e401.
68 S. Lopez-Marino, M. Espíndola-Rodríguez, Y. Sánchez, X. Alcobé, F. Oliva, H. Xie, M. Neuschitzer, S. Giraldo, M. Placidi, R. Caballero, V. Izquierdo-Roca, A. Pérez-Rodríguez and E. Saucedo, *Nano Energy*, 2016, **26**, 708–721.
69 Q. Yu, J. Shi, L. Guo, B. Duan, Y. Luo, H. Wu, D. Li and Q. Meng, *Nano Energy*, 2020, **76**, 105042.
70 B. Shin, Y. Zhu, N. A. Bojarczuk, S. Jay Chey and S. Guha, *Appl. Phys. Lett.*, 2012, **101**, 053903.
71 Y. Zeng, Z. Shen, X. Wu, D.-X. Wang, Y.-L. Wang, Y.-L. Sun, L. Wu and Y. Zhang, *J. Materiomics*, 2021, **7**, 470–477.
72 X. Min, L. Guo, Q. Yu, B. Duan, J. Shi, H. Wu, Y. Luo, D. Li and Q. Meng, *Sci. China Mater.*, 2018, **62**, 797–802.
73 A. Zhang, Z. Zhou, W. Zhou, D. Kou, Y. Meng, Y. Qi, S. Yuan and S. Wu, *Sol. RRL*, 2019, **3**, 1900131.
74 X. Sun, L. Yu, F. Yang, X. Dong, J. Chen, X. Zhang, Y. Zhao and Y. Li, *Sol. Energy Mater. Sol. Cells*, 2022, **248**, 112034.

75 G. Yan, C. Zeng, Y. Yuan, G. Wang, G. Cen, L. Zeng, L. Zhang, Y. Fu, C. Zhao, R. Hong and W. Mai, *ACS Appl. Mater. Interfaces*, 2019, **11**, 32097–32107.
76 S. Y. Kim, S. H. Kim, S. Hong, D. H. Son, Y. I. Kim, S. Kim, K. Ahn, K. J. Yang, D. H. Kim and J. K. Kang, *ACS Appl. Mater. Interfaces*, 2019, **11**, 23160–23167.
77 Y. Gong, Y. Zhang, Q. Zhu, Y. Zhou, R. Qiu, C. Niu, W. Yan, W. Huang and H. Xin, *Energy Environ. Sci.*, 2021, **14**, 2369–2380.
78 L. Guo, J. Shi, Q. Yu, B. Duan, X. Xu, J. Zhou, J. Wu, Y. Li, D. Li, H. Wu, Y. Luo and Q. Meng, *Sci. Bull.*, 2020, **65**, 738–746.
79 C. Niu, Y. Gong, R. Qiu, Q. Zhu, Y. Zhou, S. Hao, W. Yan, W. Huang and H. Xin, *J. Mater. Chem. A*, 2021, **9**, 12981–12987.
80 H. Cui, C.-Y. Lee, W. Li, X. Liu, X. Wen and X. Hao, *Int. J. Photoenergy*, 2015, **2015**, 1–9.
81 H. Cui, X. Liu, F. Liu, X. Hao, N. Song and C. Yan, *Appl. Phys. Lett.*, 2014, **104**, 041115.
82 C. M. Sutter-Fella, J. A. Stückelberger, H. Hagendorfer, F. La Mattina, L. Kranz, S. Nishiwaki, A. R. Uhl, Y. E. Romanyuk and A. N. Tiwari, *Chem. Mater.*, 2014, **26**, 1420–1425.
83 H. Zhou, T. B. Song, W. C. Hsu, S. Luo, S. Ye, H. S. Duan, C. J. Hsu, W. Yang and Y. Yang, *J. Am. Chem. Soc.*, 2013, **135**, 15998–16001.
84 T. Prabhakar and N. Jampana, *Sol. Energy Mater. Sol. Cells*, 2011, **95**, 1001–1004.
85 T. Maeda, A. Kawabata and T. Wada, *Phys. Status Solidi C*, 2015, **12**, 631–637.
86 X. Chang, J. Fu, D. Kou, W. Zhou, Z. Zhou, S. Yuan, Y. Qi, Z. Zheng and S. Wu, *J. Mater. Chem. A*, 2021, **9**, 413–422.
87 K. J. Yang, S. Kim, S. Y. Kim, D. H. Son, J. Lee, Y. I. Kim, S. J. Sung, D. H. Kim, T. Enkhbat, J. Kim, J. Kim, W. Jo and J. K. Kang, *Adv. Funct. Mater.*, 2021, **31**, 2102238.
88 Y. Sun, H. Guo, P. Qiu, S. Zhang, S. Wang, L. Wu, J. Ao and Y. Zhang, *J. Energy Chem.*, 2021, **57**, 618–626.
89 S. Sahayaraj, G. Brammertz, B. Vermang, A. Mule, T. Schnabel, M. Meuris, J. Vleugels and J. Poortmans, *J. Mater. Chem. A*, 2018, **6**, 2653–2663.
90 J. Kim, G. Y. Kim, T. T. T. Nguyen, S. Yoon, Y. K. Kim, S. Y. Lee, M. Kim, D. H. Cho, Y. D. Chung, J. H. Lee, M. J. Seong and W. Jo, *Phys. Chem. Chem. Phys.*, 2020, **22**, 7597–7605.
91 D. A. R. Barkhouse, R. Haight, N. Sakai, H. Hiroi, H. Sugimoto and D. B. Mitzi, *Appl. Phys. Lett.*, 2012, **100**, 193904.
92 R. Haight, A. Barkhouse, O. Gunawan, B. Shin, M. Copel, M. Hopstaken and D. B. Mitzi, *Appl. Phys. Lett.*, 2011, **98**, 253502.
93 C. Yan, F. Liu, N. Song, B. K. Ng, J. A. Stride, A. Tadich and X. Hao, *Appl. Phys. Lett.*, 2014, **104**, 173901.
94 S. Wang, Z. Shen, Y. Sun, H. Li, K. Zhang, L. Wu, J. Ao and Y. Zhang, *ACS Appl. Mater. Interfaces*, 2021, **13**, 12211–12220.
95 Z.-K. Yuan, S. Chen, H. Xiang, X.-G. Gong, A. Walsh, J.-S. Park, I. Repins and S.-H. Wei, *Adv. Funct. Mater.*, 2015, **25**, 6733–6743.
96 J. Ramanujam, D. M. Bishop, T. K. Todorov, O. Gunawan, J. Rath, R. Nekovei, E. Artegiani and A. Romeo, *Prog. Mater Sci.*, 2020, **110**, 100619.
97 W. Wang, M. T. Winkler, O. Gunawan, T. Gokmen, T. K. Todorov, Y. Zhu and D. B. Mitzi, *Adv. Energy Mater.*, 2014, **4**, 1301465.
98 Y. S. Lee, T. Gershon, T. K. Todorov, W. Wang, M. T. Winkler, M. Hopstaken, O. Gunawan and J. Kim, *Adv. Energy Mater.*, 2016, **6**, 1600198.
99 J. Park, J. Huang, J. Yun, F. Liu, Z. Ouyang, H. Sun, C. Yan, K. Sun, K. Kim, J. Seidel, S. Chen, M. A. Green and X. Hao, *Adv. Energy Mater.*, 2018, **8**, 1701940.
100 X. Cui, K. Sun, J. Huang, J. S. Yun, C.-Y. Lee, C. Yan, H. Sun, Y. Zhang, C. Xue, K. Eder, L. Yang, J. M. Cairney, J. Seidel, N. J. Ekins-Daukes, M. Green, B. Hoex and X. Hao, *Energy Environ. Sci.*, 2019, **12**, 2751–2764.
101 F. Jiang, C. Ozaki, Gunawan, T. Harada, Z. Tang, T. Minemoto, Y. Nose and S. Ikeda, *Chem. Mater.*, 2016, **28**, 3283–3291.
102 K. Sun, C. Yan, F. Liu, J. Huang, F. Zhou, J. A. Stride, M. Green and X. Hao, *Adv. Energy Mater.*, 2016, **6**, 1600046.
103 J. Lee, T. Enkhbat, G. Han, M. H. Sharif, E. Enkhbayar, H. Yoo, J. H. Kim, S. Kim and J. Kim, *Nano Energy*, 2020, **78**, 105206.
104 K. Sun, C. Yan, J. Huang, F. Liu, J. Li, H. Sun, Y. Zhang, X. Cui, A. Wang, Z. Fang, J. Cong, Y. Lai, M. A. Green and X. Hao, *J. Mater. Chem. A*, 2019, **7**, 27289–27296.
105 K. Sun, J. Huang, C. Yan, A. Pu, F. Liu, H. Sun, X. Liu, Z. Fang, J. A. Stride, M. Green and X. Hao, *Chem. Mater.*, 2018, **30**, 4008–4016.
106 F. Liu, C. Yan, J. Huang, K. Sun, F. Zhou, J. A. Stride, M. A. Green and X. Hao, *Adv. Energy Mater.*, 2016, **6**, 1600706.
107 S. Gao, Y. Zhang, J. Ao, X. Li, S. Qiao, Y. Wang, S. Lin, Z. Zhang, D. Wang, Z. Zhou, G. Sun, S. Wang and Y. Sun, *Sol. Energy Mater. Sol. Cells*, 2018, **182**, 228–236.
108 C. Yan, J. Huang, K. Sun, S. Johnston, Y. Zhang, H. Sun, A. Pu, M. He, F. Liu, K. Eder, L. Yang, J. M. Cairney, N. J. Ekins-Daukes, Z. Hameiri, J. A. Stride, S. Chen, M. A. Green and X. Hao, *Nat. Energy*, 2018, **3**, 764–772.
109 Y. Gong, Y. Zhang, E. Jedlicka, R. Giridharagopal, J. A. Clark, W. Yan, C. Niu, R. Qiu, J. Jiang, S. Yu, S. Wu, H. W. Hillhouse, D. S. Ginger, W. Huang and H. Xin, *Sci. China Mater.*, 2020, **64**, 52–60.
110 W. Wu, Y. Cao, J. V. Caspar, Q. Guo, L. K. Johnson, R. S. McLean, I. Malajovich and K. R. Choudhury, *Appl. Phys. Lett.*, 2014, **105**, 042108.
111 H. Sun, K. Sun, J. Huang, C. Yan, F. Liu, J. Park, A. Pu, J. A. Stride, M. A. Green and X. Hao, *ACS Appl. Energy Mater.*, 2017, **1**, 154–160.
112 J. Eun Song, S. Kyung Hwang, J. Hyun Park and J. Young Kim, *ChemSusChem*, 2022, **15**, e202102350.
113 X. Zhang, Z. Zhou, L. Cao, D. Kou, S. Yuan, Z. Zheng, G. Yang, Q. Tian, S. Wu and S. Liu, *Adv. Funct. Mater.*, 2022, **33**, 2211315.
114 J. Li, D. Wang, X. Li, Y. Zeng and Y. Zhang, *Adv. Sci.*, 2018, **5**, 1700744.

115 L. Grenet, F. Emieux, J. Andrade-Arvizu, E. De Vito, G. Lorin, Y. Sánchez, E. Saucedo and F. Roux, *ACS Appl. Energy Mater.*, 2020, **3**, 1883–1891.
116 K. F. Tse, S. Wang, M. H. Wong and J. Zhu, *J. Semicond.*, 2022, 43.
117 A. Santoni, F. Biccari, C. Malerba, M. Valentini, R. Chierchia and A. Mittiga, *J. Phys. D: Appl. Phys.*, 2013, **46**, 175101.
118 A. Nagoya, R. Asahi and G. Kresse, *J. Phys. Condens. Matter*, 2011, **23**, 404203.
119 A. Crovetto, C. Yan, B. Iandolo, F. Zhou, J. Stride, J. Schou, X. Hao and O. Hansen, *Appl. Phys. Lett.*, 2016, **109**, 233904.
120 J. Y. Cho, J. S. Jang, V. C. Karade, R. Nandi, P. S. Pawar, T.-J. Seok, W. Moon, T. J. Park, J. H. Kim and J. Heo, *J. Alloys Compd.*, 2022, **895**, 162651.
121 S. Wang, Z. Jiang, Z. Shen, Y. Sun, H. Guo, L. Wu, J. Zhang, J. Ao, H. Wang and Y. Zhang, *Sci. China Mater.*, 2020, **64**, 288–295.
122 H. Jeong, R. Nandi, J. Y. Cho, P. S. Pawar, H. S. Lee, K. E. Neerugatti, J. H. Kim and J. Heo, *Prog. Photovoltaics Res. Appl.*, 2021, **29**, 1057–1067.
123 M. Nguyen, K. Ernits, K. F. Tai, C. F. Ng, S. S. Pramana, W. A. Sasangka, S. K. Batabyal, T. Holopainen, D. Meissner, A. Neisser and L. H. Wong, *Sol. Energy*, 2015, **111**, 344–349.
124 J. Y. Park, R. B. V. Chalapathy, A. C. Lokhande, C. W. Hong and J. H. Kim, *J. Alloys Compd.*, 2017, **695**, 2652–2660.
125 F. Liu, C. Yan, K. Sun, F. Zhou, X. Hao and M. A. Green, *ACS Photonics*, 2017, **4**, 1684–1690.
126 Z. Xu, Q. Gao, C. Cui, S. Yuan, D. Kou, Z. Zhou, W. Zhou, Y. Meng, Y. Qi, M. Ishaq, U. A. Shah and S. Wu, *Adv. Funct. Mater.*, 2022, **33**, 2209187.
127 B. Duan, L. Lou, F. Meng, J. Zhou, J. Wang, J. Shi, H. Wu, Y. Luo, D. Li and Q. Meng, *ACS Appl. Mater. Interfaces*, 2021, **13**, 55243–55253.